Interplay between appearance and disappearance channels for precision measurements of θ_{23} and δ

Pilar Coloma,[1,*] Hisakazu Minakata,[2,†] and Stephen J. Parke[3,‡]

[1]*Center for Neutrino Physics, Virginia Tech, Blacksburg, Virginia 24061, USA*
[2]*Instituto de Física, Universidade de São Paulo, C.P. 66.318, 05315-970 São Paulo, Brazil*
[3]*Theoretical Physics Department, Fermi National Accelerator Laboratory, P.O. Box 500, Batavia, Illinois 60510, USA*

(Received 3 July 2014; published 11 November 2014)

We discuss how the *CP*-violating phase δ and the mixing angle θ_{23} can be measured precisely in an environment where there are strong correlations between them. This is achieved by paying special attention to the mutual roles and the interplay between the appearance and the disappearance channels in long-baseline neutrino oscillation experiments. We analyze and clarify the general structure of the $\theta_{23} - \theta_{13} - \delta$ degeneracy for both the appearance and disappearance channels in a more complete fashion than what has previously been discussed in the literature. A full understanding of this degeneracy is of vital importance if θ_{23} is close to maximal mixing. The relative importance between the appearance and disappearance channels depends upon the particular setup and how close to maximal mixing nature has chosen the value for θ_{23}. For facilities that operate with a narrow band beam or a wideband beam centered on the first oscillation extremum, the contribution of the disappearance channel depends critically on the systematic uncertainties assumed for this channel, whereas for facilities that operate at energies above the first oscillation extremum or at the second oscillation extremum, the appearance channels dominate. On the other hand, for δ we find that the disappearance channel usually improves the sensitivity, modestly for facilities around the first oscillation extremum and more significantly for facilities operating at an energy above the first oscillation extremum, especially near $\delta \sim \pm\pi/2$.

DOI: 10.1103/PhysRevD.90.093003 PACS numbers: 14.60.Lm, 14.60.Pq

I. INTRODUCTION

The three flavor mixing angles in the lepton sector are all measured now, and the next step is to measure the *CP*-violating phase δ [1]. It would be the last step, aside from determination of the neutrino mass hierarchy, to complete our understanding of lepton mixing in the standard three-generation scheme. Lepton *CP* violation is one of the indispensable ingredients for leptogenesis [2] which could explain baryon number asymmetry in the Universe.

At the same time, neutrino physics is entering the precision era. Precision will help successful model building in the leptonic sector, which eventually should lead to the resolution of the so-called flavor puzzle. Fortunately, θ_{13} will be soon determined accurately by the Daya Bay and the other reactor experiments [3–5], which is free from the uncertainties on θ_{23} and δ [6]. Given the high accuracy of θ_{12} measurement by the solar [7] (see also, e.g., [8] for a review on results from solar oscillation experiments) and the KamLAND [9] experiments, which may be even more improved at the JUNO [10] or RENO-50 [11] experiments, θ_{23} will be the least precisely known mixing angle. Then, the uncertainty of θ_{23} could be one of the dominant sources of uncertainty for the measurement of δ, in addition to statistical and systematic ones.

Up to now, it is generally assumed that θ_{23} will mainly be determined through ν_μ disappearance measurements, and δ is to be measured by ν_e and $\bar{\nu}_e$ appearance measurements, possibly simultaneously with θ_{13}, or with a given measured value of θ_{13} by reactor experiments. However, it turns out that the problem of determining θ_{23} and δ simultaneously is not that simple.

If θ_{23} is close to maximal mixing, i.e., $\sin^2 2\theta_{23} \gtrsim 0.96$ (a value to which the experimental results seem to be converging), the determination of $\sin^2\theta_{23}$ will be difficult, because the two allowed regions for θ_{23} (the true solution and one clone) merge together [12]. As a result, the final allowed region for $\sin^2\theta_{23}$ will span both the first and second octants of θ_{23}. It was shown that the ν_e and $\bar{\nu}_e$ appearance measurements by themselves, no matter how accurate, produce a continuous "tusk-shaped" degeneracy line, parameterized by the value of δ, in $\sin^2\theta_{13}$–$\sin^2\theta_{23}$ space [6]. Though the three-dimensional $\theta_{23} - \theta_{13} - \delta$ parameter space is squeezed by the reactor measurement of θ_{13} (yet with finite resolution), we still have to deal with the problem of determining θ_{23} and δ simultaneously [13]. We will see that it suffers from a parameter degeneracy involving θ_{23}, θ_{13}, and δ.

We utilize the following four experimental setups to illuminate the characteristic features of this degeneracy:

*pcoloma@vt.edu
†hisakazu.minakata@gmail.com
‡parke@fnal.gov

(i) T2HK [14] for a representative case of setups whose neutrino spectrum is peaked near the first vacuum oscillation maximum (VOM), such that $\Delta_{31} \equiv (m_3^2 - m_1^2)L/4E = \pm\pi/2$, where L is the distance to the detector and E is the neutrino energy, (ii) LBNE [15] for a representative case of setups with wideband neutrino beams around $|\Delta_{31}| \sim (2 \pm 1)\pi/4$, (iii) neutrino factory (NF) [16,17] for a representative case of setups at higher energies than VOM, $|\Delta_{31}| \sim \pi/4$, and at long baseline with a sizable matter effect, and (iv) ESSνSB [18,19] for a representative case of setups with the neutrino spectrum peaked near the second VOM, $|\Delta_{31}| = 3\pi/2$.

The paper is structured as follows. First, we aim at illuminating the structure of the parameter degeneracy in the three-dimensional $\theta_{23} - \theta_{13} - \delta$ space, which will be denoted as the general $\theta_{23} - \theta_{13} - \delta$ degeneracy. Despite that the intrinsic θ_{13}-δ degeneracy [20] (and to less extent the intrinsic θ_{23}-δ one [13]) multiplied with the discrete θ_{23} octant degeneracy [21] (see also [22]) has been discussed extensively in the literature, to our knowledge, its full structure has never been addressed in a complete fashion. A detailed discussion of this degeneracy will be presented in Sec. II. Then, in the rest of the paper, we study how well θ_{23} and δ can be measured at future neutrino oscillation facilities, focusing in particular on the relative importance of ν_μ disappearance vs $\nu_\mu \to \nu_e$ ($\bar{\nu}_\mu \to \bar{\nu}_e$) appearance measurements[1] for a precise determination of $\sin^2\theta_{23}$ and δ. This will be discussed in Secs. IV and V, respectively. Finally, we summarize our results and present our conclusions in Sec. VI.

II. GENERAL $\theta_{23} - \theta_{13} - \delta$ DEGENERACY OF THE APPEARANCE AND DISAPPEARANCE CHANNELS

Here, we discuss the general structure of degeneracy involving θ_{23}, θ_{13}, and δ which is encountered in the measurement of these parameters. Our aim in this section is to illuminate the nature of this parameter degeneracy but not to go deeply into discussing how it can be resolved. However, we do expect that our discussion will be useful to formulate the resolution of this degeneracy. While our discussions in this section are meant to be pedagogical in nature, many of the features of this general $\theta_{23} - \theta_{13} - \delta$ degeneracy are entirely new. Clues toward formulating the general $\theta_{23} - \theta_{13} - \delta$ degeneracy have been given by many authors but within various approximations. For example, a formal degeneracy equation has been written down by Donini, Meloni, and Rigolin [23] under the $\theta_{23} \leftrightarrow \pi/2 - \theta_{23}$ approximation and by Chatterjee *et al.* [24] under restriction to a part of the three-dimensional manifold. However, the full analytical structure of these degeneracies has not been revealed in a manner which is as general as that presented in this paper, nor have they ever been analyzed, imposing a clear discrimination between the degeneracies of the appearance and disappearance channels.

For the sake of simplicity, we will assume throughout this paper that the neutrino mass hierarchy is known to be the normal hierarchy. In the case of unknown mass hierarchy, the number of allowed solutions would be doubled, since the clone solutions would also appear for the wrong mass hierarchy [25]. The extension can be done in a straightforward manner. Finally, the inclusion of matter effects complicates the discussion without adding too much to the understanding. Therefore we will turn them off in the rest of this section.

A. Observables and overview

In this paper, we consider the following four observables in discussing the determination of θ_{23}, θ_{13}, and δ:

(1) $P_{\mu e}(\theta_{23}, \theta_{13}, \delta)$ and $\bar{P}_{\mu e}(\theta_{23}, \theta_{13}, \delta)$.—the appearance oscillation probabilities[2] for $\nu_\mu \to \nu_e$ and $\bar{\nu}_\mu \to \bar{\nu}_e$, respectively. For these probabilities there is a continuous degeneracy in the three variables θ_{23}, θ_{13}, and δ. We will refer to this degeneracy as the "$\theta_{23} - \theta_{13} - \delta$ appearance degeneracy."

(2) $P_{\mu\mu}(\theta_{23}, \theta_{13})$.—the disappearance oscillation probability for $\nu_\mu \to \nu_\mu$. For this probability there is a continuous degeneracy in the two variables θ_{23} and θ_{13}. We will refer to this degeneracy as the "$\theta_{23} - \theta_{13}$ disappearance degeneracy."

(3) $\bar{P}_{ee}(\theta_{13})$.—the disappearance oscillation probability for $\bar{\nu}_e \to \bar{\nu}_e$. There is no degeneracy in this channel, since $\cos^2\theta_{13}$ is not small and therefore θ_{13} is determined unambiguously. [See the discussion after Eq. (3).]

In this section, we restrict ourselves to the analytic treatment of the degeneracy assuming measurements of the above observables for a fixed neutrino energy E. Since there are four equations for the three variables, the system is, in general, overconstrained, and, in principle, there is no degeneracy if each measurement is precise enough except at possible isolated values of the neutrino energy. However, degeneracies may appear if the measurements are not accurate enough.

Let us start by discussing what has been addressed in the literature up to now regarding the degeneracies associated with $\theta_{23} - \theta_{13} - \delta$.

(a) If a ν_μ disappearance measurement of $\sin^2 2\theta_{23}$ is sufficiently accurate to determine θ_{23} (up to its octant), then a set of ν_e and $\bar{\nu}_e$ appearance measurements

[1]Here, and in the rest of this work, we denote the appearance channels for the superbeam experiments with the implicit understanding that for the neutrino factory or beta beam experiments the appearance channels are $\nu_e \to \nu_\mu$ and its CP conjugate.

[2]Here only the variables which have an important effect in our discussion are shown as arguments of the oscillation probabilities. Explicit expressions for the oscillation probabilities will be given below.

would give two allowed solutions for (θ_{13}, δ): the true solution and a degenerate one, which has been referred to as "θ_{13} intrinsic degeneracy" [20]. Moreover, one would get two solutions for each value of θ_{23}; thus, this degeneracy is fourfold (eightfold if we consider that the sign of Δm^2_{31} is unknown).

(b) If the accuracy in determining $\sin^2\theta_{13}$ overwhelms that of $\sin^2\theta_{23}$, which is more or less the case after the reactor measurement of θ_{13}, a set of ν_e and $\bar{\nu}_e$ appearance measurements would give two allowed solutions for (θ_{23}, δ): the true solution and a degenerate one, which has been referred to as the "θ_{23} intrinsic degeneracy" [13]. In this case, the degeneracy is twofold excluding the ambiguity of the mass hierarchy.

In the first case, (a) above, the resultant fourfold degeneracy has been described as a direct product of the θ_{13} intrinsic and the θ_{23} octant degeneracies, whereas the second case (b) is a θ_{23} intrinsic degeneracy which could, in principle, be resolved by an accurate determination of $\sin^2\theta_{23}$ from a ν_μ disappearance experiment. However, if θ_{23} is near maximal mixing ($\sim\frac{\pi}{4}$), this is challenging due to the Jacobian involved in translating the measured variable $\sin^2 2\theta$ to $\sin^2\theta$.

The general $\theta_{23}-\theta_{13}-\delta$ degeneracy we discuss here is best considered to be made up of two separate degeneracies: one associated with the appearance channels, the $\theta_{23}-\theta_{13}-\delta$ appearance degeneracy, and the second associated with the ν_μ disappearance channel, the $\theta_{23}-\theta_{13}$ disappearance degeneracy. Both these degeneracies are continuous in the associated variables and will be illuminated in more detail in the following subsections.

B. Appearance channels and the $\theta_{23}-\theta_{13}-\delta$ appearance degeneracy

We start by describing the ν_e and $\bar{\nu}_e$ appearance measurements to understand the structure of $\theta_{23}-\theta_{13}-\delta$ appearance degeneracy. We will show that both the θ_{23} and the θ_{13} intrinsic degeneracies can be identified as particular projections of this appearance degeneracy.

The ν_e and $\bar{\nu}_e$ appearance oscillation probabilities can be written as

$$\begin{aligned} P(\nu_\mu\to\nu_e) &= (s_{23}\sin 2\theta_{13})^2 A_\oplus^2 + 2\epsilon(s_{23}\sin 2\theta_{13})(c_{23}c_{13})A_\oplus A_\odot\cos(\delta+\Delta_{31}) + \epsilon^2(c_{23}c_{13})^2 A_\odot^2, \\ P(\bar{\nu}_\mu\to\bar{\nu}_e) &= (s_{23}\sin 2\theta_{13})^2 \bar{A}_\oplus^2 + 2\epsilon(s_{23}\sin 2\theta_{13})(c_{23}c_{13})\bar{A}_\oplus A_\odot\cos(\delta-\Delta_{31}) + \epsilon^2(c_{23}c_{13})^2 A_\odot^2, \end{aligned} \tag{1}$$

where $\Delta_{ij}\equiv\frac{\Delta m^2_{ij}L}{4E}$ and $\epsilon\equiv\frac{\Delta m^2_{21}}{\Delta m^2_{31}}\simeq 0.03$. The A functions in (1) are defined[3] as

$$\begin{aligned} A_\oplus &\equiv \left(\frac{\Delta m^2_{31}}{\Delta m^2_{31}-a}\right)\sin\left[\frac{(\Delta m^2_{31}-a)L}{4E}\right], \\ \bar{A}_\oplus &\equiv \left(\frac{\Delta m^2_{31}}{\Delta m^2_{31}+a}\right)\sin\left[\frac{(\Delta m^2_{31}+a)L}{4E}\right], \\ A_\odot &\equiv \sin 2\theta_{12}\left(\frac{\Delta m^2_{31}}{a}\right)\sin\left(\frac{aL}{4E}\right) = \bar{A}_\odot. \end{aligned} \tag{2}$$

Here, $a=2\sqrt{2}G_F N_e E$, where G_F is the Fermi constant, N_e is the electron density in matter, and E is the neutrino energy.

1. The appearance degeneracy and the relationship to the intrinsic degeneracies

If we solve Eq. (1) for θ_{23} and θ_{13} by eliminating δ at a given neutrino energy E and a baseline L, a curve on the $\sin^2\theta_{13}$ vs $\sin^2\theta_{23}$ plane results. An example of such a curve is drawn in vacuum in the left panel of Fig. 1 by varying δ for a setup with $L=295$ km and a neutrino energy of 1 GeV. That is, if we set up the problem so that we obtain solutions for θ_{23} and θ_{13} by measurement of $P\equiv P(\nu_\mu\to\nu_e)$ and $\bar{P}\equiv P(\bar{\nu}_\mu\to\bar{\nu}_e)$ at a certain value of energy, we have solutions on any points on the curve; the degeneracy is continuous. In other words, because of the freedom of adjusting θ_{13} and θ_{23} to reproduce the measurement points $(P,\bar{P})$, the solutions are in fact not only at the discrete points but on a continuous line parameterized by δ, e.g., θ_{23} expressed as a function of θ_{13} as in the left panel of Fig. 1. The correlation between θ_{13} and θ_{23}, which has been noticed in simulation studies since early times, e.g., in [26], seems to reflect at least partly the effect of the tusk-shaped correlation displayed in the left panel of Fig. 1.

To reveal the features of the appearance degeneracy and to understand its relationship to the θ_{23} and θ_{13} intrinsic degeneracies, let us do the following exercise. Suppose that the true values of the parameters are at $\sin^2\theta_{23}=0.4$, $\sin^2\theta_{13}=0.02$, and $\delta=40°$ as indicated by the black star in the left panel of Fig. 1. If we know θ_{13} exactly, we have a clone solution at $\sin^2\theta_{23}^{(2)}=0.5$, $\sin^2\theta_{13}^{(2)}=0.02$, and $\delta^{(2)}=140°$, as indicated by the blue star. This is nothing but an example of the θ_{23} intrinsic degeneracy. Notice that $\delta^{(2)}=\pi-\delta$ as it should be in vacuum, whereas if we know θ_{23} exactly, we have the third solution shown by the red star in Fig. 1 at $\sin^2\theta_{23}^{(3)}=0.4$, $\sin^2\theta_{13}^{(3)}=0.0255$, and $\delta^{(3)}=146°$, an example of the θ_{13} intrinsic degeneracy. A similar description of how appearance and disappearance measurements can solve the θ_{23} disappearance "octant" degeneracy with figures like the one in the left panel of Fig. 1 appeared in [6,27].

[3]Our definition of the A functions differs from that of Ref. [13].

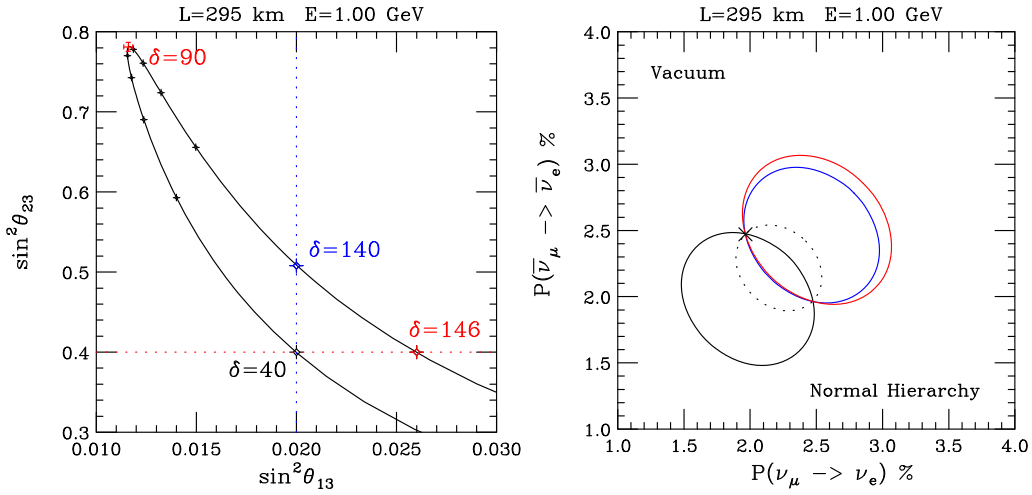

FIG. 1 (color online). Left panel: Set of points in the $\sin^2\theta_{13}$-$\sin^2\theta_{23}$ plane which simultaneously give $P(\nu_\mu \to \nu_e) \approx 0.02$ and $P(\bar{\nu}_\mu \to \bar{\nu}_e) \approx 0.025$ in vacuum, for $E_\nu = 1$ GeV and $L = 295$ km. Each point in the curve corresponds to a different value of δ. Larger stars on the curve mark the points corresponding to the θ_{23} and θ_{13} intrinsic degeneracy solutions. Small stars indicate values of δ in steps of 10°, from 40° to 140°. Notice the accumulation of points $\delta = 80°$, 90°, and 100° near the tip of the tusk. Right panel: The biprobability plot in $P(\nu_\mu \to \nu_e)$ vs $P(\bar{\nu}_\mu \to \bar{\nu}_e)$ space. The points with large stars on the curve in the left panel correspond to the ellipses with the same color in the right panel. The dotted curve is the smallest ellipse that can be drawn through these points.

The fact that each degenerate solution is able to reproduce the measured quantities ($P \approx 0.02$ and $\bar{P} \approx 0.025$ in this particular case) can be easily seen if we use the biprobability plot in $P - \bar{P}$ space [25]. In the right panel of Fig. 1, the three biprobability ellipses corresponding to the three degenerate solutions (the true point and two fake clones) are drawn by using the same color as used in the left panel.[4]

2. $\theta_{23} - \theta_{13} - \delta$ appearance degeneracy is fragile

It has been recognized that the θ_{13} and the θ_{23} intrinsic degeneracies are "fragile" in the sense that the position of the fake solutions is energy dependent so that spectrum measurements can be used to rule them out. It is worth noting that this fragility continues to be true for the $\theta_{23} - \theta_{13} - \delta$ appearance degeneracy. In Fig. 2, the position of the appearance degeneracy is shown for different values of L/E. As can be seen, the position of the appearance degeneracies changes as the value of L/E is varied. However, there is one common solution for all four values L/E of the experiment, which is of course the unique true solution. Thus, spectral information will be particularly valuable for eliminating the fake solutions provided there is ample statistics in each of the energy bins. This may be contrasted to the feature of disappearance "octant" degeneracy (see Sec. II C) for which the clone solution is L/E independent.

To close this subsection, we emphasize that the $\theta_{23} - \theta_{13} - \delta$ appearance degeneracy, for the three parameters θ_{23}, θ_{13}, and δ, is a continuous degeneracy of the combined ν_e and $\bar{\nu}_e$ appearance probabilities only.

C. Disappearance channels and the $\theta_{23} - \theta_{13}$ disappearance degeneracy

In this short subsection, we summarize the degeneracy issues for both the ν_μ and ν_e disappearance channels. Much of what is contained here already exists in the literature in a scattered way (see, e.g., Ref. [28] for a detailed discussion of the ν_μ disappearance degeneracy in the case of large θ_{13}); we include it here so that the reader and the authors are on the same page and to set the notation that we will use throughout this paper.

Reactor electron antineutrino disappearance experiments with baselines appropriate to observer atmospheric oscillations, such as the Daya Bay [3], RENO [5], and Double Chooz [4] experiments, have values of $L/E \sim$ 0.5 km/MeV. They measure the oscillation probability $P(\bar{\nu}_e \to \bar{\nu}_e)$:

$$P(\bar{\nu}_e \to \bar{\nu}_e) = 1 - \sin^2 2\theta_{13} \sin^2\left(\frac{\Delta m^2_{ee} L}{4E}\right) + O(\Delta^2_{21}), \quad (3)$$

[4]The reader may wonder about the meaning of the dotted ellipse in the right panel of Fig. 1. It is the special case with the smallest size of the ellipse. There is a unique way to draw the minimum size ellipse passing through the measurement point $(P, \bar{P})$. Namely, it is to place the ellipse so that its edge just touches the point $(P, \bar{P})$ as marked by the cross in the right panel of Fig. 1. Since the upper-left edge of the ellipse always corresponds to $\delta = 90°$, the solution must correspond to this value of δ. Since this ellipse is unique by definition, there is no degeneracy in this case. Therefore, the point $\delta = 90°$ must be at the tip of the tusk, as shown by the red star in the left panel of Fig. 1.

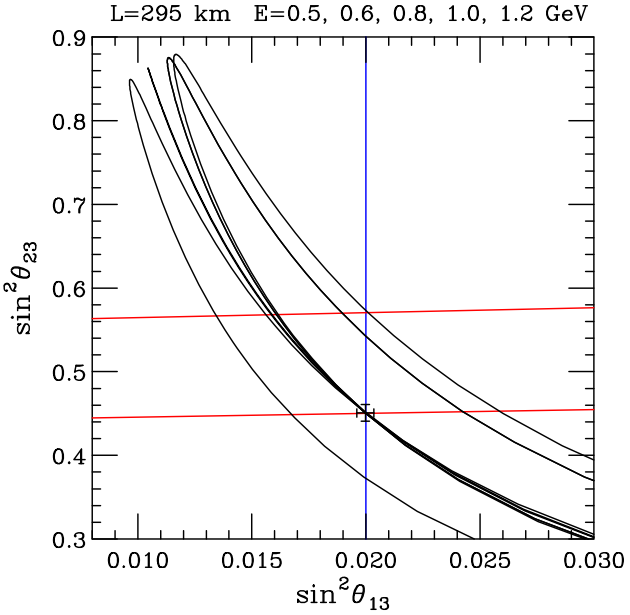

FIG. 2 (color online). The appearance measurement degeneracy for four different neutrino energies, from left to right, 0.50, ~0.6, 0.80, and 1.00 GeV using a baseline of 295 km. The true input value (black cross) corresponds to $\sin^2\theta_{23} = 0.45$, $\sin^2\theta_{13} = 0.020$, and $\delta = 30°$. The black curve for $E \sim 0.6(0.58)$ GeV is special, because it corresponds to the VOM for this baseline, $\Delta_{31} = \pi/2$. Therefore, the biprobability ellipses are squashed to a line, and the degeneracy folds over upon itself. This figure clearly shows that this degeneracy is fragile in the sense of being dependent on L/E. The vertical blue line is given by $\sin^2\theta_{13} = 0.020$, and the, almost horizontal, red lines show the solutions corresponding to $\sin^2 2\theta_{\mu\mu} = 0.986$; see the next subsection. Note that the appearance degeneracy line for an energy of 1.0 GeV passes through both intersection points of the fixed $\sin^2\theta_{13}$ and fixed $\sin^2 2\theta_{\mu\mu}$ constraints.

where Δm^2_{ee} is the electron neutrino weighted average of Δm^2_{31} and Δm^2_{32} [29]. In principle, there is an octant degeneracy here for θ_{13}, since the measurement of $\sin^2 2\theta_{13}$ does not allow one to distinguish θ_{13} from $\pi/2 - \theta_{13}$. However, the Super-Kamiokande (Super-K) atmospheric neutrino results [30] ($|U_{\mu 3}|^2 = \cos^2\theta_{13}\sin^2\theta_{23} \approx 1/2$) imply that θ_{13} is relatively small (and therefore in the first octant). This results in an unambiguous, precise measurement of θ_{13}:

$$\sin^2\theta_{13} \approx 0.023. \tag{4}$$

For the muon neutrino disappearance experiments at the atmospheric baseline divided by neutrino energy, $L/E \sim 500$ km/GeV, such as K2K [31], MINOS [32], T2K [33], and NOνA [34], the muon neutrino survival probability is given by

$$P(\nu_\mu \to \nu_\mu) = 1 - \sin^2 2\theta_{\mu\mu}\sin^2\left(\frac{\Delta m^2_{\mu\mu} L}{4E}\right) + O(\Delta^2_{21}), \tag{5}$$

where $\Delta m^2_{\mu\mu}$ is the muon neutrino weighted average of Δm^2_{31} and Δm^2_{32} [29], and

$$\begin{aligned}\sin^2 2\theta_{\mu\mu} &\equiv 4|U_{\mu 3}|^2(1 - |U_{\mu 3}|^2) \\ &= 4\cos^2\theta_{13}\sin^2\theta_{23}(1 - \cos^2\theta_{13}\sin^2\theta_{23}).\end{aligned} \tag{6}$$

Matter effects are very small in this channel (except maybe for some neutrino factory setups), and are ignored here.

For relatively small values of θ_{13}, the fate of the determination of $\sin^2\theta_{23}$ depends very much on how close θ_{23} is to the maximal value. In Fig. 3, we have plotted the χ^2 of $\sin^2 2\theta_{\mu\mu}$ as a function of $\sin^2\theta_{23}$ assuming an uncertainty of 1.4% for the labeled various central values for $\sin^2 2\theta_{\mu\mu}$. Using this uncertainty, the two regions start to merge when $\sin^2 2\theta_{\mu\mu} > 0.96$ and the determination of $\sin^2\theta_{23}$ from the ν_μ disappearance measurements is significantly degraded. It should be noted that the merged region displayed in the two rightmost panels in Fig. 3 is very similar to that can be seen in the global fits, Refs. [35–37]. (The critical value which separates the two regions, of course, will depend on the actual accuracy of the measurement.)

A measurement of $\sin^2 2\theta_{\mu\mu}$ gives two distinct values of $\sin^2\theta_{23}$ given by [28]

$$\begin{aligned}\sin^2\theta^{(1)}_{23} &= \sin^2\theta_{\mu\mu}/\cos^2\theta_{13} \approx \sin^2\theta_{\mu\mu}(1 + \sin^2\theta_{13}), \\ \sin^2\theta^{(2)}_{23} &= \cos^2\theta_{\mu\mu}/\cos^2\theta_{13} \approx \cos^2\theta_{\mu\mu}(1 + \sin^2\theta_{13}),\end{aligned} \tag{7}$$

using the convention that $\theta_{\mu\mu} \le \frac{\pi}{4}$, i.e., $\sin^2\theta_{\mu\mu} \le \frac{1}{2}$. Note that $\theta^{(2)}_{23}$ is *always* in the second octant, and, for *nearly all* values of $\theta_{\mu\mu}$, $\theta^{(1)}_{23}$ is in the first octant. However, if

$$\sin^2\theta_{\mu\mu} > \frac{1}{2}\cos^2\theta_{13},$$

then $\theta^{(1)}_{23}$ is *also* in the second octant. This new feature of the θ_{23} "octant" degeneracy occurs only if θ_{23} is very close to maximal and for the observed nonzero value of θ_{13}.

For $\sin^2 2\theta_{23} \simeq \sin^2 2\theta_{\mu\mu} \gtrsim 0.96$, the two allowed regions of $\sin^2\theta_{23}$ merge to a unique one which is extended to both the first and the second octants of θ_{23}. Exactly where this occurs depends on the systematic errors used in the disappearance measurement. An example is shown in the right panel of Fig. 3. In this merged region, information on the value of $\sin^2\theta_{23}$ from the appearance channels will be particularly useful.

What is currently known about $\sin^2 2\theta_{\mu\mu}$? The recent ν_μ disappearance measurement by T2K reported $\sin^2 2\theta_{\mu\mu} \gtrsim 0.97$ at 90% C.L. [1 degree of freedom (DOF)] [33,38]. Thus, it appears that nature has chosen to live in this merged region, on which we focus in the following discussion.

To close this subsection, we emphasize that this $\theta_{23} - \theta_{13}$ disappearance degeneracy (or "octant" degeneracy), for

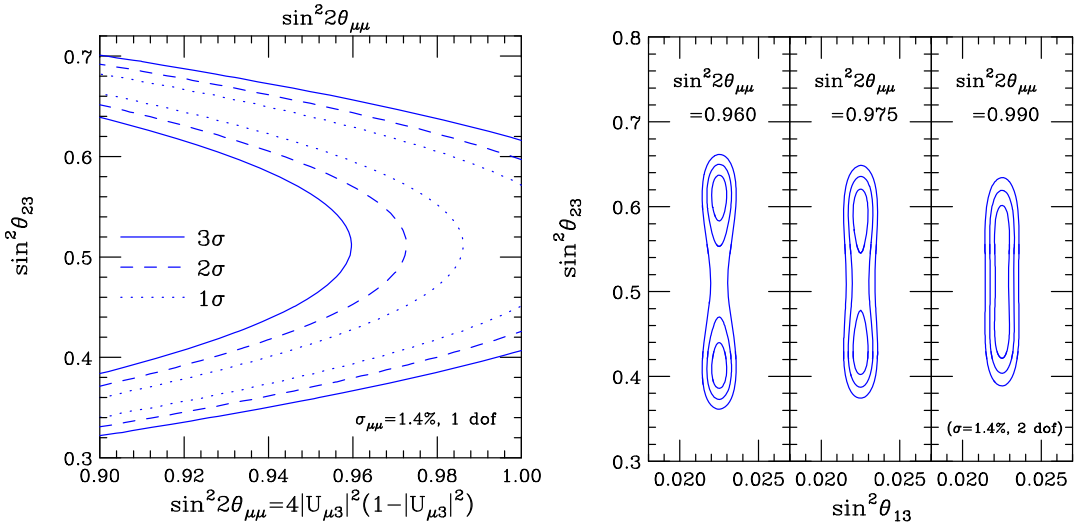

FIG. 3 (color online). Left panel: Contours for the χ^2 distribution in the $\sin^2 2\theta_{\mu\mu}$-$\sin^2\theta_{23}$ plane, where $\chi^2 \equiv (4\cos^2\theta_{13}\sin^2\theta_{23}(1-\cos^2\theta_{13}\sin^2\theta_{23})-\sin^2 2\theta_{\mu\mu})^2/(\sigma_{\mu\mu}\sin^2 2\theta_{\mu\mu})^2$, $\sin^2\theta_{13}=0.023$, and $\sigma_{\mu\mu}=1.4\%$. Right panel: Contours for the same χ^2 in the $\sin^2\theta_{13}$ and $\sin^2\theta_{23}$ plane, for different values of $\sin^2 2\theta_{\mu\mu}$ as indicated in each subpanel. With the assumed uncertainty, there are two distinct allowed bands for $\sin^2\theta_{23}$ for values of $\sin^2 2\theta_{\mu\mu} < 0.96$, whereas the two bands start to merge for $\sin^2 2\theta_{\mu\mu} > 0.96$. Note the small upward shift with respect to the line $\sin^2\theta_{23}=0.5$ caused by the nonzero value of $\sin^2\theta_{13}$. In both panels, the different lines correspond to different confidence levels as indicated in the legend. Note that the left panel corresponds to 1 DOF, while the right panel is obtained for 2 DOF.

the two parameters θ_{23} and θ_{13}, is a continuous degeneracy of the ν_μ disappearance probability only.

D. Features of the general $\theta_{23}-\theta_{13}-\delta$ continuous degeneracy

In the merged region $\sin^2 2\theta_{\mu\mu} \gtrsim 0.96$, we face two kinds of continuous degeneracies: the $\theta_{23}-\theta_{13}-\delta$ appearance degeneracy and the $\theta_{23}-\theta_{13}$ disappearance degeneracy. In this subsection, we discuss some of the interesting features of these degeneracies and their intersection.[5]

In Fig. 4, the allowed regions in the $\sin^2\theta_{23}-\sin^2\theta_{13}$ plane are shown for 2σ C.L. (2 DOF). The vertical blue band comes from the $\bar{\nu}_e$ disappearance measurement, the almost horizontal red band corresponds to the merged first and second octant solutions for the ν_μ disappearance measurements, and the dotted black band is the $\nu_\mu \to \nu_e$ and $\bar{\nu}_\mu \to \bar{\nu}_e$ appearance measurements. In all cases, the uncertainties on the measurement are assumed to be of 1.4% and are implemented as in Ref. [13]. This figure clearly shows the continuous degeneracy in the $\sin^2\theta_{23}$ vs $\sin^2\theta_{13}$ plane associated with the appearance and disappearance probabilities, as well as the overlapping regions

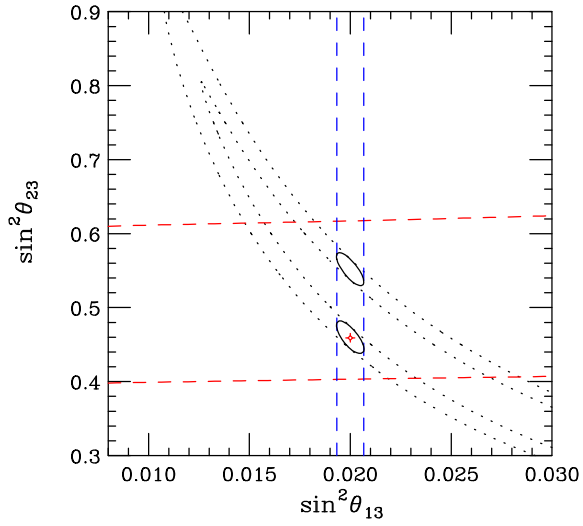

FIG. 4 (color online). Allowed confidence regions in the $\sin^2\theta_{13}$-$\sin^2\theta_{23}$ plane at the 2σ C.L. (2 DOF), using different oscillation channels, for an experiment with a baseline of 295 km and a (monochromatic) neutrino energy of 0.8 GeV (i.e., $\Delta_{31} \sim 3\pi/8$). The allowed region for the appearance $\nu_\mu \to \nu_e$ and $\bar{\nu}_\mu \to \bar{\nu}_e$ measurements is given by the dotted black bands. The vertical blue and (almost) horizontal red bands indicate the regions allowed by the ν_e and ν_μ disappearance measurements constraints on $\sin^2 2\theta_{13}$ and $\sin^2 2\theta_{\mu\mu}$. Finally, the solid black ellipses are the overlap regions for these three types of measurements.

[5]We note that the previous discussions of the relationship between the appearance and disappearance degeneracies, for example, in [6,27], did not address the continuous nature of the disappearance degeneracy.

between them. One of these overlapping regions is the true solution, while the other region is fake and will move as we vary the neutrino energy.[6]

The assumed true input values for the oscillation parameters in this case are

$$\sin^2\theta_{23} = 0.45, \quad \sin^2\theta_{13} = 0.020, \quad \text{and} \quad \delta = 30°. \quad (8)$$

This is represented in this figure by the black solid lines with the red cross in the center. The other region which also satisfies all the measurements is located at a larger value of $\sin^2\theta_{23}$. Its exact position will depend on the value of L/E for the experiment, and it will be located at a value of $\delta^{(2)} = \pi - \delta$. This second solution will move up and down within the vertical blue band between the two sets of horizontal red lines depending on the neutrino energy, as it was shown in Fig. 2. Thus, spectral information would be very powerful in removing this degeneracy, provided the statistics is sufficient in several well-defined energy bins.

III. EXPERIMENTAL SETUPS

Four experimental setups are considered in this work. We believe these are representative of four different types of neutrino oscillation experiments, according to their values of L/E. As it stands, the nature of the four settings to be examined is not intended for a performance comparison between the different setups but to illuminate their characteristic features based on different physical principles.

(1) *Narrow band beams operating at the first VOM*, $\Delta_{31} \sim \pi/2$.—The beam is aimed to the detector at an off-axis location, so that the flux is very narrow in energy, centered around the first VOM. This is the case of T2K [39] and NOνA [34], for instance. In this work, we will consider an upgrade of T2K, which is usually referred to as T2HK [14]. It will use the same beam line as T2K uses, aiming instead at a 560 kt fiducial volume water Čerenkov detector Hyper-Kamiokande (Hyper-K) to be placed at the same distance (295 km) and off-axis angle (2.5°) as Super-K.

(2) *Wideband beams operating around the first VOM, i.e.,* $\Delta_{31} \sim (2 \pm 1)\pi/4$.—These experiments are performed on axis. Therefore, the beam flux is much wider than in the previous case, and as a consequence they observe not only the first VOM but also some regions above and below it. The main advantage of this type of experiment is that the oscillation pattern is much better reconstructed and the statistics is much larger since the detector is placed on axis. Examples of this type of experiment are LBNE [15,40,41] and LBNO [42]. In this work, we will consider the LBNE experiment, which consists of a 1.2 MW beam and a 34 kt liquid argon (LAr) detector placed underground, at a baseline of 1300 km from the source.

(3) *Neutrino beams operating below VOM, i.e.*, $\Delta_{31} < \pi/2$.—The NF setups traditionally considered in the literature would operate in this regime; see, for instance, Ref. [43]. More recently, lower energy versions have also been proposed; see, for instance, [16,44,45], which operate in a regime much closer to the first VOM. In this work, we will consider a NF setup operating below VOM, such as the IDS-NF setup [17], with a baseline of 2000 km and a parent muon neutrino energy of $E_\mu = 10$ GeV [16]. For this setup, we consider a 100 kt magnetized iron neutrino detector (MIND).

(4) *Neutrino beams operating at the second VOM, i.e.*, $\Delta_{31} = 3\pi/2$.—This is the case of the recently proposed ESSνSB facility in Europe [18,19]. At the second VOM, the size of the δ-dependent interference term between the atmospheric and the solar terms is a factor of ∼3 larger than that at the first VOM, which would lead to higher sensitivity to δ. The favorable feature is utilized in this and in the earlier proposals, e.g., in [46–49]. Here, we consider one of the setups within the ESSνSB proposal, which consists of a 500 kt fiducial mass water Čerenkov detector placed at 540 km from the source. As for the beam, we will consider a 5 MW beam produced by using 2.5 GeV protons.

Table I summarizes the main features of the setups considered in this work. The different columns indicate the baseline, neutrino flux peak, beam power per year (or number of useful muon decays, in the case of the IDS-NF), detector size, and data-taking period for neutrinos and antineutrinos. Technical details used to simulate each setup, as well as the number of events for each oscillation channel, can be found in Appendix A, together with a brief explanation of the χ^2 implementation, the inclusion of systematic errors in our analysis, the values of the oscillation parameters, and the marginalization procedure.

IV. APPEARANCE AND DISAPPEARANCE MEASUREMENTS OF θ_{23}

Given the understanding of mutual roles played by the ν_e appearance and the ν_μ disappearance channels in resolving

[6]These two solutions, which stem from the appearance degeneracy, could have been misunderstood as a consequence of the disappearance "octant" degeneracy, if the appearance and disappearance channels are analyzed simultaneously to obtain the allowed regions. This can be understood from Fig. 2 as well. It can be seen in Fig. 2 that, at $\sin^2\theta_{13} = 0.02$, the appearance degeneracy curve with $E = 1.0$ GeV has two allowed solutions for $\sin^2\theta_{23}$: the true one (indicated by a black cross), plus an appearance clone solution which overlaps with the disappearance (octant) clone. However, such an overlap occurs only for isolated values of the neutrino energy.

TABLE I. Main features of the experimental setups simulated in this work. The different columns indicate the distance to the detector, the detector technology, its mass, the beam power (or the number of useful muon decays per year in the case of the IDS-NF), the energy at which the neutrino flux peaks, and the running time (in units of 10^7 s) for ν and $\bar{\nu}$ modes. Here, LAr stands for liquid argon, WC for water Čerenkov, and MIND for magnetized iron neutrino detector. Note also that in the case of the IDS-NF the energies for the flux peak for both ν_e and $\bar{\nu}_\mu$ (in parenthesis) are separately indicated, since they are different. For the number of events in each oscillation channel, see Table II.

	L (km)	Detector (kt)	Beam power	E_p (GeV)	Flux peak	$(t_\nu, t_{\bar{\nu}})^{a} \times 10^7$ s
LBNE	1300	LAr - 34	1.2 MW	120	3 GeV	(8.25, 8.25)
T2HK	295	WC - 560	0.75 MW	30	0.6 GeV	(3, 7)
ESSνSB	540	WC - 500	5 MW	2.5	0.3 GeV	(3.4, 13.6)
IDS-NF	2000	MIND - 100	10^{21} $\mu^{\pm}/10^7$ s	NA	6 (9) GeV	(10, 10)[b]

[a]Note that each experiment assumes a different number of operating seconds per calendar year. LBNE and ESSνSB assume $\sim 1.7 \times 10^7$ operating s/y, while T2HK and IDS-NF assume 1.0×10^7 operating s/y. This implies that the running time for all the experiments considered in this work is expected to be 10 calendar years.

[b]While for conventional beams the running time is split between neutrino (π^+-focusing) and antineutrino (π^--focusing) modes, the IDS-NF setup assumes that both μ^+ and μ^- would run at the same time in the decay ring. The total number of muon decays per year would be equally split between the two polarities in this case.

the general $\theta_{23} - \theta_{13} - \delta$ degeneracy, we now discuss more closely their relative importance in accurate measurement of θ_{23} and how it depends on the systematic errors. The answer to this question depends on the particular setup under consideration. Therefore, we focus on the two typical cases T2HK/LBNE and IDS-NF in Secs. IV A and IV B, respectively. We will also comment briefly on the results for the ESSνSB experiment. In Sec. IV C, we discuss the relationship between errors of $\sin^2\theta_{23}$ and $\sin\delta$ using the appearance measurement only.

We note that the issue of the mutual role by the appearance and disappearance channels for θ_{23} determination has been addressed, e.g., in [50–52]. More generally, the sensitivity to θ_{23} has been discussed, though from a somewhat different point of view, by many authors. The analyses from early to recent times include, for example, Refs. [12,24,27,53–60].

Finally, some remarks should be given at this point about global fits to neutrino oscillation data. Global fits may also be able to determine the values of θ_{23} and δ; see Refs. [35–37] for recent results and detailed discussions on the topic. In principle, this could be achievable from the combination of reactors and neutrino beam data alone. However, such a combination is not precise enough yet, and both octants for θ_{23} are currently allowed. Atmospheric neutrino data may be able to lift this degeneracy, although they are not precise enough yet to give a significant determination of the octant for θ_{23}. Finally, the combination of reactor and neutrino beam experimental data may be able to provide a significant hint for the value of δ. From the combination of reactors and T2K neutrino data, global fits already get a hint for $\delta \sim 1.5\pi$ (although with a low statistical significance yet). It should be taken into account, though, that a determination of the value of δ from global fits using the *current* generation of experiments may be possible only for particular combinations of θ_{23}, the neutrino mass ordering, and the value of δ itself. Therefore, a deep understanding of the possible ways to lift these degeneracies through the combination of appearance and disappearance data is necessary in order to optimize future neutrino facilities towards a simultaneous determination of θ_{23} and δ. This is the main purpose of the present work.

A. Relative importance of appearance and disappearance channels for facilities sitting at the first VOM: T2HK and LBNE

In this subsection, we discuss the precision that can be achieved for a measurement of $\sin^2\theta_{23}$ with the disappearance and/or the appearance channels for facilities sitting at the first VOM and discuss their dependence with the systematic errors. The results of the analyses are presented in Figs. 5 and 6 for the T2HK and LBNE setups, respectively. In both figures, we show the precision attainable for a measurement of $\sin^2\theta_{23}$ as a function of the true value of $\sin^2\theta_{23}$ itself, where the left and right panels show the results under different assumptions for the systematic errors. In the left panel, we use our default values ($\sim$5%–10%), while more conservative values are assumed for the right panel ($\sim$10%–15%). See Appendix A for a more precise specification of the systematic errors and the way these are implemented in our analysis.[7]

[7]The size of the expected systematic errors for future neutrino oscillation experiments can be a controversial subject and is currently under study. For T2HK we have used the systematic uncertainties based on the HK letter of intent (LoI) [14], and for LBNE they fall approximately within the same ballpark as those considered by the Collaboration (see, e.g., Ref. [15]). We note that the systematic errors for ν_e appearance measurement currently examined by the Hyper-K working group [61] are more optimistic than our default values. In this case, the appearance sensitivity (solid line) in the left panel in Fig. 5 would supersede the disappearance one around $\sin^2\theta_{23} \sim 0.49$ and $\sin^2\theta_{23} \sim 0.54$, recovering region II.

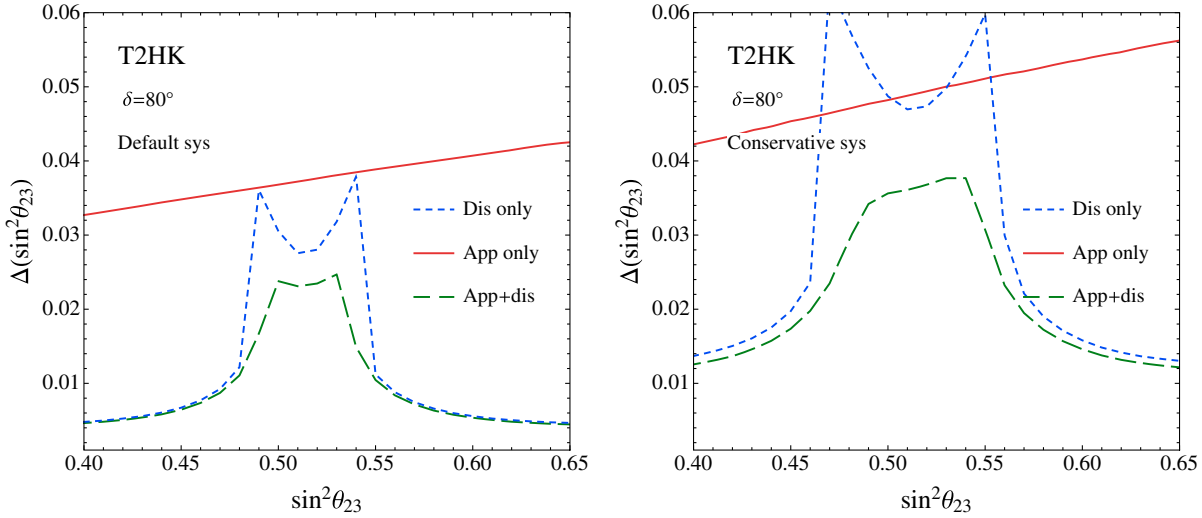

FIG. 5 (color online). Expected precision for $\sin^2\theta_{23}$ at 1σ (1 DOF) as a function of the true value of $\sin^2\theta_{23}$ for the T2HK setup. The left and the right panels correspond to our reference (∼5%–10%) and conservative (∼10%–15%) sets of systematic errors, respectively. See Appendix A for more precise specification of the reference errors. The true value of δ is taken as 80°.

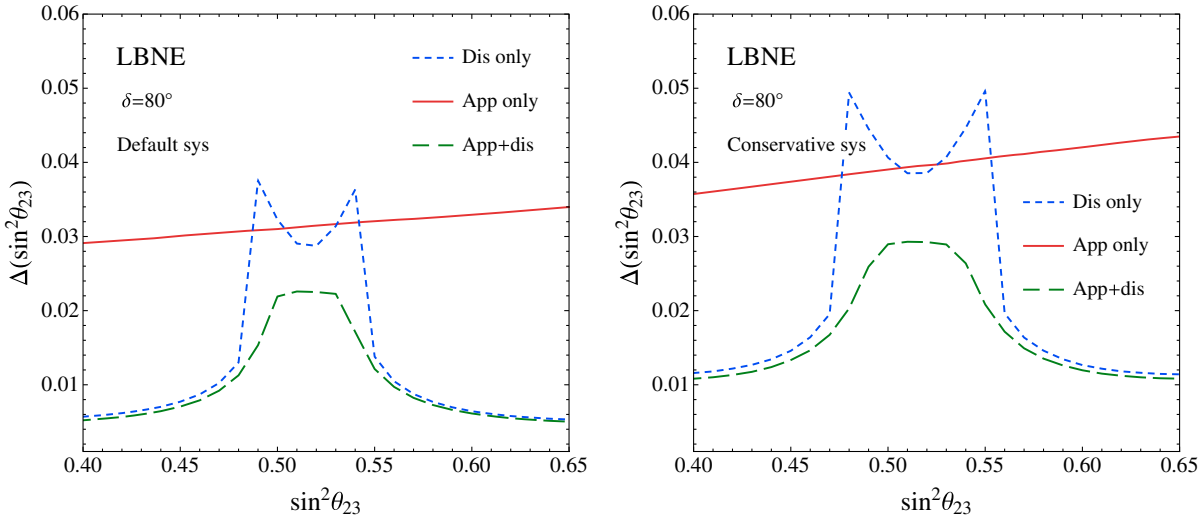

FIG. 6 (color online). The same as in Fig. 5, but for the LBNE setup.

As can be seen from the figures, not only the absolute sensitivity to $\sin^2\theta_{23}$ but also the relative importance of ν_e appearance and ν_μ disappearance measurement on the determination of θ_{23} depend very much on the size of the systematic errors. It is notable that not only this feature but also the absolute sensitivities to $\sin^2\theta_{23}$ (for our default systematic errors) are very similar between the T2HK and LBNE setups, despite their very different beam profiles and detector technologies. Yet, one observes that the LBNE setup would be more robust against the increase of systematic errors, probably because of its wideband beam.[8]

The very different dependence of the results is also quite noticeable for the different oscillation channels with the true value of θ_{23}. The results obtained through the appearance channels present very little dependence with this parameter for both LBNE and T2HK. On the other hand, the disappearance results present a very particular shape, with two very sharp peaks. This is due to the disappearance degeneracy (see Sec. II): For values of θ_{23} close to maximal mixing the two solutions merge, and the size of the confidence region is consequently worsened; the "valley" in the middle of the two peaks corresponds to the point where the two solutions lie exactly one on top of the other, and therefore the precision is slightly improved. We can identify, generically, the following three regions with

[8]Similar conclusions were obtained in Ref. [62] for different observables.

different characteristics. We note, however, that the exact locations of the boundaries between regions depend on the systematic and the statistical errors.

Region I.—In the two regions where $\sin^2\theta_{23} \lesssim 0.46$ or $\sin^2\theta_{23} \gtrsim 0.55$, the ν_μ disappearance measurement has the leading power to determine $\sin^2\theta_{23}$ very accurately, apart from the disappearance "octant" degeneracy.

Region II.—In a limited region inside $0.46 \lesssim \sin^2\theta_{23} \lesssim 0.55$, excluding a small region around $\sin^2\theta_{23} = 0.5$, the ν_e appearance measurement can constrain $\sin^2\theta_{23}$ better than the disappearance one. For particular combinations of the systematic errors in the appearance and disappearance channels, this region may be absent, though (see, for instance, the left panel in Fig. 5). The precise boundaries of this region with regions I and III (see below) depend very much on the size of the systematic errors, as one can see from Fig. 5.

Region III.—For values of $\sin^2\theta_{23}$ very close to maximal, a third region appears, in which the disappearance measurement again supersedes the appearance measurement. As explained above, this is due to overlapping of the two clones when they are very close to maximal mixing.

Overall, one can see from Figs. 5 and 6 that ν_e appearance and ν_μ disappearance measurements cooperate to determine $\sin^2\theta_{23}$ very accurately, with a 1σ uncertainty 0.02–0.03, or ~5% level, which is comparable to the possible ultimate accuracy for $\sin^2\theta_{13}$ expected from reactor experiments. If θ_{23} is in region I, the error may be even smaller. We note, however, that regions II and III are the ones to which the experimental results seem to be converging [33].

B. Appearance vs disappearance channels in neutrino factory setting

The relative importance of appearance and disappearance channels in the determination of θ_{23} is quite different for the IDS-NF setup. As shown in Fig. 7, region III does not exist in this case, while region II is quite wide: $0.44 \lesssim \sin^2\theta_{23} \lesssim 0.59$. Since the setting we consider for the neutrino factory is off VOM, the disappearance measurement is not as powerful as for facilities sitting at the first VOM like T2HK or LBNE. Also, note that the general features shown in Fig. 7 are rather robust against variation of the systematic errors in the disappearance channel within a reasonable range, since for the NF this channel is mainly limited by being off peak.

Finally, we have also examined the ESSνSB setting with a baseline of 540 km. Unfortunately, neither the disappearance nor the appearance measurement have sufficient statistics to determine $\sin^2\theta_{23}$ with a comparable accuracy to any of the other settings discussed above. For example, the appearance-only measurement can reach only up to $\Delta(\sin^2\theta_{23}) \sim 0.07$ at $\sin^2\theta_{23} = 0.5$ for various input values of δ.

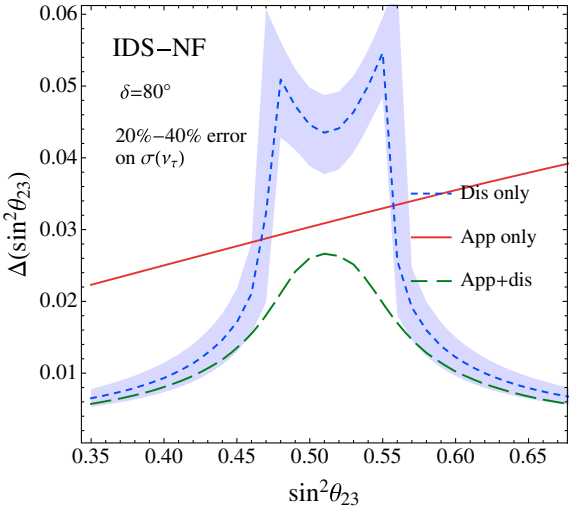

FIG. 7 (color online). The same as the left panel in Fig. 5, but for the IDS-NF setup. All lines correspond to the assumed uncertainty for this parameter in our default scenario (30%), while the blue band shows the impact on the result for the disappearance channels if the systematic error on the ν_τ cross section is varied between 20% and 40%.

C. Accuracy of measurements: $\sin^2\theta_{23}$ vs $\sin\delta$

Starting from simple analytical considerations, a simple expression relating the precision achievable for $\sin^2\theta_{23}$ and $\sin\delta$ using *only* the appearance channel at the first VOM was derived in Ref. [13]:

$$\Delta(\sin^2\theta_{23}) \simeq \frac{1}{6}\Delta(\sin\delta). \tag{9}$$

We have confirmed that this relation holds reasonably well when both observables are computed within the same experimental setup sitting near the VOM. The results are shown in Fig. 8 for the case of the T2HK setup. In this figure, the uncertainty on $\sin\delta$ is compared to the uncertainty on $\sin^2\theta_{23}$ multiplied by a factor of 6. Results are shown as a function of the value of δ itself, for $\sin^2\theta_{23} = 0.50$. As can be seen from the figure, the agreement between the two curves is quite good, and they show a similar dependence with the value of δ itself, with the sole exception of the regions close to $\pm\pi/2$.

The reason for the disagreement in these two regions can be partially explained by taking into account that the function $\sin\delta$ in these regions has an upper limit, while this is not the case for $\sin^2\theta_{23}$ in the region under consideration (i.e., around maximal mixing). Therefore, one should expect the confidence interval in this region to be reduced by approximately a factor of 2 for $\sin\delta$. It is also related to the Jacobian involved in the measurement of $\sin\delta$, as partially discussed in Ref. [63]. The precision on $\sin\delta$ can be computed by doing a Taylor expansion by $\Delta(\delta)$, the uncertainty on δ. To first order in the expansion, it

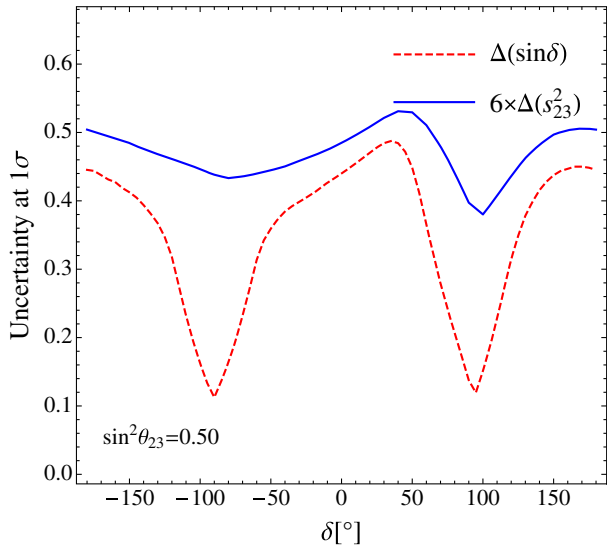

FIG. 8 (color online). Comparison between the precision achievable for $\sin^2\theta_{23}$ and the precision achievable for $\sin\delta$ for the T2HK setup. The solid line shows the error on $\sin^2\theta_{23}$ multiplied by a factor of 6, while the dashed lines show the error on $\sin\delta$ as obtained directly from a simulation. The agreement between the two curves is noticeable in most of the δ parameter space, as predicted by Eq. (9), which was derived from simple analytical considerations in Ref. [13] for facilities sitting at the first VOM. It should be noted that in this figure the *full* size of the confidence interval is plotted in both cases, unlike for the rest of the figures in this paper, where we show half of the size of the full confidence interval.

gives $\Delta(\sin\delta) = \cos\delta\Delta(\delta)$, which implies that $\Delta(\sin\delta)$ should vanish at $\delta = \pm\frac{\pi}{2}$. When higher order terms are included in the Taylor expansion, however, a nonvanishing result is obtained, in agreement with the minima for the dashed curve in Fig. 8.

We have also examined whether the relation holds for different values of θ_{23}. The qualitative features of the results are quite similar, but the difference between the solid blue and the dashed red curves in Fig. 8 becomes larger: It increases by approximately a factor of ~ 3 at $\delta = 0$ when θ_{23} is varied from $\sin^2\theta_{23} = 0.40$ to $\sin^2\theta_{23} = 0.60$, while they are more similar near the dips ($\delta \sim \pm\pi/2$).

V. DETERMINATION OF δ

Let us now explore what the impact is due to the combination of different channels on the determination of δ. Figure 9 shows the expected precision for a measurement of δ for the T2HK (LBNE) experiment in the left (right) panel, as a function of the value of δ itself. Results are shown at 1σ C.L., for 1 DOF. As one can see, the addition of the disappearance channels is helping to get a better determination of δ, especially in the regions around $\delta = \pm\pi/2$, as was already pointed out in Refs. [51,63]. This effect comes mainly through a better determination of the squared mass splitting in the ν_μ disappearance channels, which can be understood from the fact that δ and Δm^2_{31} appear together in the appearance oscillation probability; see Eq. (1).

The left panel in Fig. 10 shows similar results for the IDS-NF setup. The improvement on the determination of δ after the addition of disappearance channel data is remarkable for this setup. In the right panel in the same figure, we show the confidence regions at 1σ (2 DOF) projected in the $\sin^2\theta_{23} - \delta$ plane. Results are shown for the appearance channels alone (red region, solid line), disappearance channels alone (blue region, dotted line), and for the combination of appearance and disappearance channels (green region, dashed line). From this panel, it can be clearly seen how the measurement of θ_{23} is coming mainly from the appearance channel for this setup, while the accurate determination of δ stems from the combination between appearance and disappearance data.

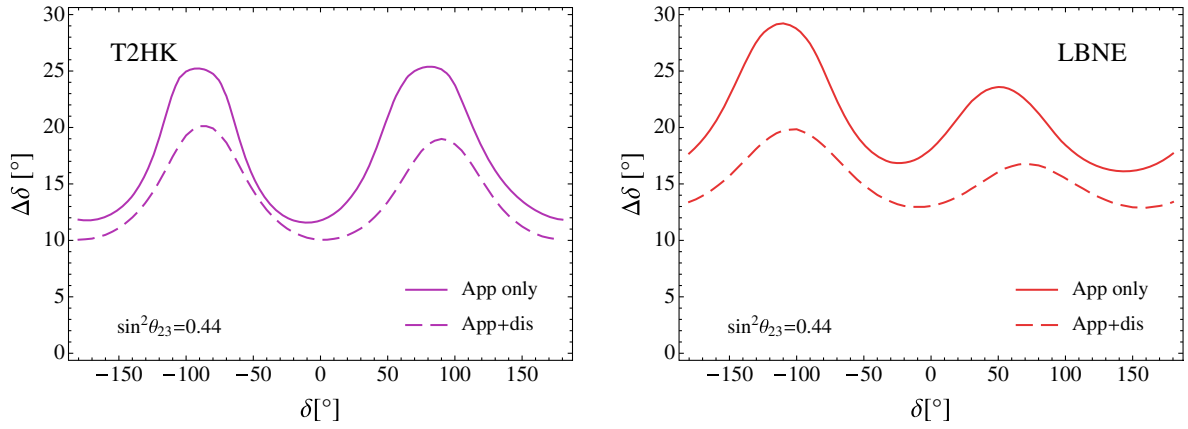

FIG. 9 (color online). Precision on δ (at 1σ, for 1 DOF) as a function of the value of δ itself, for T2HK in the left panel and for LBNE in the right panel. Solid lines show the results using the appearance channels only, while dashed lines show the results from the combination of appearance and disappearance data.

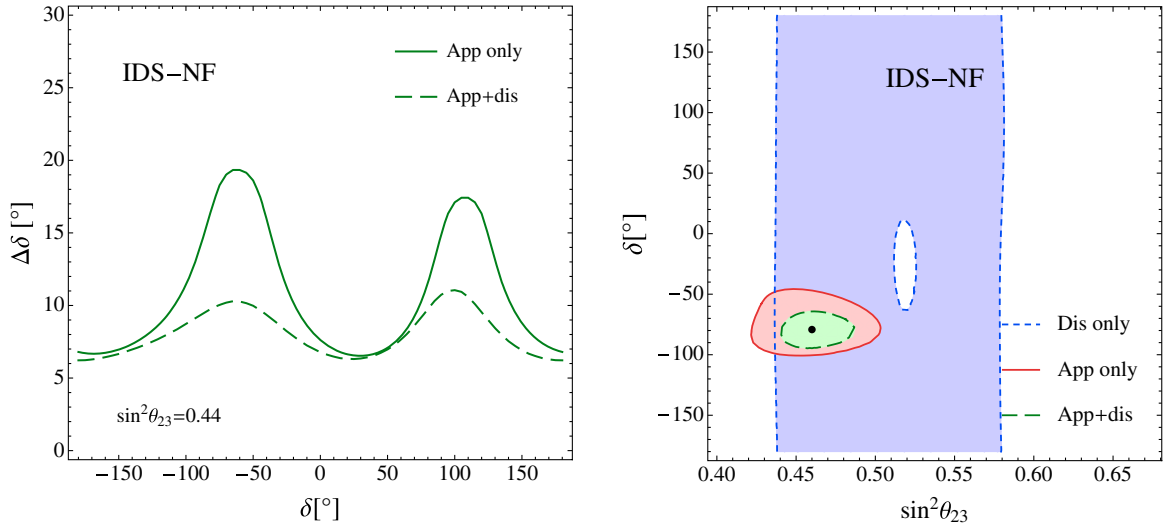

FIG. 10 (color online). Left panel: Expected precision on δ (at 1σ, for 1 DOF) as a function of the value of δ itself, for the IDS-NF setup. Solid and dashed lines indicate the results obtained from the appearance results alone and from the combination between appearance and disappearance data, respectively. Right panel: Confidence regions in the $\sin^2\theta_{23} - \delta$ plane (at 1σ, for 2 DOF), for a particular set of true values and for different combinations of oscillation channels, as indicated in the legend. Results in both panels correspond to the IDS-NF setup as defined in Sec. III. It should be pointed out that the "hole" in the confidence region obtained for the disappearance channels vanishes just above the 1σ C.L.

The last case under study in this section is the case of ESSνSB, for which the situation is very different from all the previous cases: The much smaller number of events at this facility would not allow one to determine Δm^2_{31} very precisely. Therefore, it is expected *a priori* that for facilities operating at the second VOM the addition of disappearance data would be of little help in improving the accuracy of a measurement of δ. This is confirmed by the results shown in the left panel of Fig. 11, the precision for δ obtained from appearance data alone (solid lines) and in combination with disappearance data (dashed lines). It is remarkable that, in spite of a factor of $\sim$50 smaller number of appearance events in the ESSνSB than in IDS-NF (see Table II) setups, the sensitivity to δ using only the appearance channel data

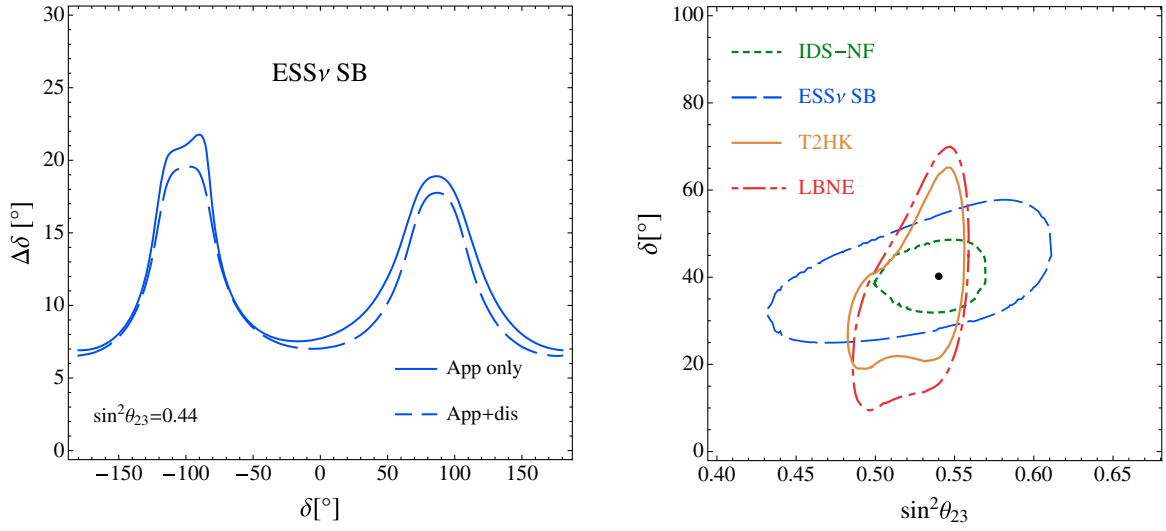

FIG. 11 (color online). Left panel: Expected precision on δ (at 1σ, for 1 DOF) as a function of the value of δ itself for the ESSνSB setup. Solid and dashed lines indicate the results obtained from the appearance results alone and from the combination between appearance and disappearance data, respectively. Right panel: Confidence regions in the $\sin^2\theta_{23} - \delta$ plane (at 1σ, for 2 DOF), for a particular set of true values (indicated by the black dot) and for the four setups considered in this work. See Tables I and II for a precise definition of the different setups and for the expected number of events in each oscillation channel, respectively. In this panel, all regions include data from both appearance and disappearance channels.

TABLE II. Number of events for the four setups considered in this work. The number of events for the signal or background component are given separately for each oscillation channel within a given setup, and detector efficiencies have already been accounted for. These event rates correspond to the following set of oscillation parameters: $\theta_{12} = 32°$, $\theta_{13} = 9°$, $\theta_{23} = 45°$, $\Delta m^2_{21} = 7.6 \times 10^{-5}$ eV^2, and $\Delta m^2_{31} = 2.45 \times 10^{-3}$ eV^2 (normal ordering of neutrino masses).

	Energy range	ν app.	$\bar{\nu}$ app.	ν dis.	$\bar{\nu}$ dis.
LBNE	0.5–8.0 GeV	1095/314	324/208	7340/82	3873/27
T2HK	0.4–1.2 GeV	3984/1705	2161/1928	26237/716	19232/735
ESSνSB	0.1–1.0 GeV	270/85	244/82	6198/113	4128/79
IDS-NF	0.1–9.0 GeV	20241/476	5257/269	171133/7370	106077/3279

is comparable with each other. It is the power of placing the detector at the second VOM where the dependence of the oscillation probability with δ is larger by a factor of 3 than that at the first VOM. It leads to an extremely good *CP*-violation sensitivity as well as a very accurate determination of the value of δ and a reduced dependence on systematic errors; see Refs. [19,46,48,49].

Finally, in the right panel of Fig. 11, we show the confidence regions in the $\sin^2\theta_{23} - \delta$ plane at 1σ (2 DOF) that would be obtained from the combination of appearance and disappearance data for the four facilities under study. The true values for $\sin^2\theta_{23}$ and δ are indicated by the black dot. In all cases, our default values have been used for the systematic uncertainties; see Appendix A. The first thing that can be noticed from this plot is the very different shape of the confidence regions for the different oscillation facilities. The ESSνSB allowed region (dashed blue line) is rather wide in the $\sin^2\theta_{23}$ axis, while it gives extremely good sensitivity to δ. The T2HK (solid yellow line) and LBNE (dot-dashed red line) regions are narrower along the $\sin^2\theta_{23}$ axis due to the disappearance constraint, but the measurement of δ would be less accurate. From the shape of the confidence region, it can also be observed that the disappearance degeneracy is affecting the determination of $\sin^2\theta_{23}$. Finally, the IDS-NF setup (dotted green line) enables the most precise measurement of *both* θ_{23} and δ due to a *synergetic* combination of appearance and disappearance measurements.

VI. SUMMARY AND CONCLUSIONS

Toward the completion of our understanding of the lepton flavor mixing, the right question to pose now is how to determine θ_{23} and the *CP*-violating phase δ at the same time and how their measurements are correlated. In this paper, we have addressed these questions. We did it in the context of four particular setups for proposed future facilities: T2HK, LBNE, IDS-NF, and ESSνSB. Throughout the paper, we paid special attention to the interplay between the $\nu_\mu \to \nu_e$ and $\bar{\nu}_\mu \to \bar{\nu}_e$ appearance channels (or their T-conjugate channels for IDS-NF) and the ν_μ and $\bar{\nu}_\mu$ disappearance channels.

In the first part of this paper, we have analyzed structure of the parameter degeneracy which we would encounter in attempting a simultaneous measurement of δ and θ_{23}. Despite the large number of previous works in the literature devoted to study degeneracies in neutrino oscillations, we found that the $\theta_{23} - \theta_{13} - \delta$ degeneracy has not been discussed in a general framework, which is mandatory if θ_{23} is close to maximal, as indicated by the recent measurements. We found that the general degeneracy boils down to the *appearance* and *disappearance* degeneracies. The former is a generalization of the θ_{13} and θ_{23} intrinsic degeneracies, whereas the latter is a generalization of what is usually called the θ_{23} octant degeneracy. Moreover, if θ_{23} is near maximal, the θ_{23} disappearance degeneracies join into a single region, aggravating the problem. We have discussed its characteristic features and illustrated some properties which are useful for its resolution in Sec. II.

In the second part of this work, we have discussed the issue of appearance vs disappearance measurement towards the determination of θ_{23} and δ and, more importantly, the interplay between them. Let us start with the measurement of θ_{23} by noting some of its generic features.

(i) The precision on θ_{23} obtained from the ν_μ disappearance channels alone generally shows a strong dependence on the size of the systematic errors. This is because the measurement is systematics dominated due to the high statistics. The error on $\sin^2\theta_{23}$ always has a strong dependence on θ_{23} as well. It develops a "bowler hat" structure in the region near the maximal θ_{23}, which stems mainly from the merging clone effect, as we discussed in Sec. II. We find that, if θ_{23} is far from maximal (in region I as defined in Sec. IV), the disappearance measurement always surpasses the appearance one in accuracy of determining $\sin^2\theta_{23}$.

(ii) On the other hand, the precision on θ_{23} obtained from the ν_e and $\bar{\nu}_e$ appearance measurement alone has a much weaker dependence on θ_{23} without suffering from the merging clone issue. The error is also less dependent on the size of systematic errors, since these channels are mostly limited by statistics instead.

We have studied the interplay between the appearance and disappearance oscillation channels at four particular setups: T2HK, LBNE, IDS-NF, and ESSνSB. Their main features are summarized in Sec. III, while a more detailed

description of the experimental setups can be found in Appendix A. The expected numbers of events in each channel for all the facilities are summarized in Table II. We observe the following.

(i) *T2HK/LBNE*.—Both of these facilities have values of L/E very close to the first VOM. For both setups, the relative importance between the appearance and the disappearance channels for a precise determination of θ_{23} depends on the size of systematic errors. With reasonable estimates for the systematic uncertainties, we find that (i) if $\sin^2\theta_{23} \simeq 0.5$, the disappearance measurement gives slightly better sensitivity to $\sin^2\theta_{23}$ than appearance; (ii) for values of θ_{23} close to $\sin^2\theta_{23} \simeq 0.49$ and 0.55, typically, the appearance measurement is more powerful than disappearance in most cases. Despite their very different experimental setups, we find that both the expected accuracies as well as the features due to the interplay between the appearance and disappearance channels are very similar.

(ii) *IDS-NF*.—This setup would operate at an energy well above the first VOM. For values of $\sin^2\theta_{23}$ such that $0.45 \lesssim \sin^2\theta_{23} \lesssim 0.56$, the accuracy in the determination of θ_{23} comes mainly from the appearance channels alone, while outside the mentioned interval the measurement is mainly driven by the disappearance channels. In particular, the precision for $\sin^2\theta_{23}$ in the region very close to maximal mixing is worse than the one obtained through the appearance measurement by a factor of up to 3–4. It has to do with the fact that the value of L/E for the IDS-NF setup considered here turns out to be rather far from the oscillation maximum. Also, the disappearance measurement is largely affected by the systematic uncertainties on the τ backgrounds. We have found that the above result holds as long as the systematic errors associated to the ν_τ charged-current cross section remain above the 20%.

(iii) ESSνSB.—At the second VOM, the situation is quite different. In this case, the value of L/E is tuned to maximize the impact of the interference term in the oscillation probability in order to obtain a better sensitivity to *CP* violation. The price to pay is that the sensitivity to θ_{23} is reduced, since it would mainly come from the precision measurement of the leading order term in the probability (for which a large number of events is needed).

We have studied the interplay of the different oscillation channels also on the determination of the *CP* phase δ. Adding the disappearance channel generally improves the sensitivity to δ, with the sole exception of ESSνSB. The improvement is always largest near $\delta \sim \pm\pi/2$. All the setups benefit from the addition of disappearance data mainly by a better determination of Δm^2_{31}, which allows cleaner discrimination of the effect of δ in the appearance channels. The size of the effect depends on various factors such as the number of events in the disappearance channels and the way the systematic errors are implemented, and hence it varies with the settings.

For both the T2HK and LBNE setups considered in this work, we find that this effect is present to a similar degree, but more prominently for LBNE in particular outside the region $\delta \sim \pm\pi/2$. In the case of the IDS-NF setup, a great improvement is observed for the precision on δ as well, especially at around $\delta = \pm\pi/2$. It is evident from the right panel of Fig. 10 that the sensitivity to δ by the disappearance data itself is not impressive at all. Therefore, such a significant effect on sensitivity to δ must come from the synergy effect between the disappearance and appearance channels in the IDS-NF setup.

In the case of ESSνSB, the situation is completely different. It is the unique case that essentially no improvement on the sensitivity to δ is achieved by adding the disappearance channel data. Yet, the precision in regions around $\delta \sim 0$ and $\pm\pi$ is remarkable, a high sensitivity that can be competed with only by IDS-NF. On the other hand, the accuracy of δ determination at around $\delta \sim \pm\pi/2$ would be comparable to those of T2HK and LBNE. See Figs. 9–11. It is worth mentioning that the comparable sensitivities to δ expected for the ESSνSB and IDS-NF setups using only appearance data are achieved with a much smaller number of events (by a factor of ~50) at the former, indicating the power of the detector at the second VOM.

In conclusion, we hope that the discussions given in this paper are useful to understand the physics behind the future precision measurement of θ_{23} and δ and that we will see some of the facilities described here realized in the near future.

ACKNOWLEDGMENTS

All the authors thank NORDITA and the organizers of the workshop "NuNews: News in Neutrino Physics," where part of this work was completed, for financial support and hospitality. P. C. thanks Enrique Fernandez-Martinez for providing the files needed to simulate the ESSνSB setup. P. C. and H. M. thank the Fermilab Theory Group for hospitality during their visits. H. M. thanks Universidade de São Paulo for the great opportunity of a stay as Pesquisador Visitante Internacional. He is also partially supported by KAKENHI received through Tokyo Metropolitan University, Grant-in-Aid for Scientific Research No. 23540315, Japan Society for the Promotion of Science. S. P. acknowledges partial support from the European Union FP7 ITN INVISIBLES (Marie Curie Actions, PITN-GA-2011-289442). Fermilab is operated by the Fermi Research Alliance under Contract No. DE-AC02-07CH11359 with the U.S. Department of Energy. Also, this work has been partially supported by the U.S. Department of Energy under Grant No. DE-SC0003915.

APPENDIX A: SIMULATION DETAILS

The LBNE setup has been simulated following the Conceptual Design Report (CDR) from October 2012 [41], rescaling the beam power and detector size to the values listed in Table I. The neutrino fluxes correspond to 120 GeV protons. Data taking is set to a total of 10 years, equally split between ν and $\bar{\nu}$ modes. Migration matrices are used to account for the misreconstruction of neutral current events as charged current events at lower energies. The signal and the rest of the backgrounds are smeared in energy according to a Gaussian with $\sigma(E) = 0.15 \times \sqrt{E}$ for electron neutrinos and $\sigma(E) = 0.20 \times \sqrt{E}$ for muon neutrinos.

The T2HK setup has been simulated as in Ref. [62]. For this setup, both signal and backgrounds are reconstructed by using the migration matrices from Ref. [64]. The beam power is set to 750 kW, and data taking is 10 years, divided between ν and $\bar{\nu}$ modes as indicated in Table I. Signal and background efficiencies have been adjusted to reproduce the number of events in the HK LoI [14].[9] We have checked that our results for T2HK are roughly consistent with those in Refs. [14,61]. We have also checked that, for a reduced statistics, the results are roughly consistent with those reported by the T2K Collaboration for the determination of $\sin^2\theta_{23}$; see Ref. [33].

Regarding the ESSνSB, several possible configurations are currently under consideration. Here, we consider a setup in which the neutrino flux is produced from 2.5 GeV protons and with a baseline accurately set to the second oscillation peak. This setup is simulated as in Refs. [18,19]. The detector response is simulated by using the migration matrices from Ref. [65], which have been obtained for the MEMPHYS detector [66].

Finally, the IDS-NF setup considered here has been optimized for the large θ_{13} scenario; see Ref. [16]. This setup uses a MIND detector [67] placed at 2000 km from the source; see Table I. The MIND response is simulated by using migration matrices for all signal and background contributions [68]. Backgrounds coming from τ decays [69,70] have also been included in the analysis.

Table II shows the expected number of events for the setups described above. The two numbers in each column indicate the signal or background expected number of events, for a given setup and a given oscillation channel. Detector efficiencies have already been accounted for. In all cases, the same cross sections as in Ref. [62] have been used.

[9]Note that in the HK LoI the beam power is roughly a factor of 2 larger than the one used in this work. Nevertheless, the running time considered was a factor of 2 smaller, and therefore the total number of events should be roughly the same.

APPENDIX B: THE χ^2 AND IMPLEMENTATION OF SYSTEMATICS UNCERTAINTIES

All results in Secs. IV and V have been obtained by using GLoBES [71,72]. The implementation of systematics has been done by using a modified version of GLoBES, as in Ref. [62]. The χ^2 and systematic uncertainties are implemented as follows. For each energy bin i, a contribution to the χ^2 is computed as

$$\chi_i^2(\theta;\xi) = 2\left(T_i(\theta;\xi) - O_i + O_i \ln\frac{O_i}{T_i(\theta;\xi))}\right), \quad \text{(B1)}$$

where O_i stands for the observed (true) event rates, and

$$T_i(\theta;\xi) = [1+\xi_{\phi,i}]s_{\nu,i}(\theta) + [1+\xi_{bg,\nu,i}]b_{\nu,i} + [1+\xi_{\phi,i}+\xi_{\bar{\nu}/\nu}]s_{\bar{\nu},i}(\theta) + [1+\xi_{bg,\bar{\nu},i}]b_{\bar{\nu},i} \quad \text{(B2)}$$

corresponds to the true (fitted) event rates observed in the ith energy bin for a given oscillation channel. Here, θ indicates the dependence on the test values for the oscillation parameters. It should be noted that O_i depends only on the true values assumed for the oscillation parameters, while T_i depends on the pair of values we are testing as well as on the nuisance parameters. $\xi_{\phi,i}$ stands for the nuisance parameter associated to a combination of flux and cross section uncertainties for the signal. We take this uncertainty to be correlated between neutrinos and antineutrinos within the same oscillation channel. $\xi_{\bar{\nu}/\nu}$ is a relative normalization uncertainty included *only* in the antineutrino channels, which accounts for the difference between neutrino and antineutrino cross section uncertainties. Finally, $\xi_{bg,\nu,i}$ and $\xi_{bg,\bar{\nu},i}$ correspond to the background normalization uncertainties in the neutrino and antineutrino channels. Note that the normalization uncertainty $\xi_{\bar{\nu}/\nu}$ is correlated among all energy bins; however, the rest of the nuisance parameters are allowed to vary independently for each bin during marginalization to account for shape uncertainties.

The final χ^2 needs to be minimized over the nuisance parameters. It reads

$$\chi^2(\theta) = \min_\xi\left\{\sum_i \chi_i^2(\theta;\xi) + \left(\frac{\xi_{\phi,i}}{\sigma_\phi}\right)^2 + \left(\frac{\xi_{\bar{\nu}/\nu}}{\sigma_{\bar{\nu}/\nu}}\right)^2 + \left(\frac{\xi_{\nu,bg,i}}{\sigma_{\nu,bg}}\right)^2 + \left(\frac{\xi_{\bar{\nu},bg,i}}{\sigma_{\bar{\nu},bg}}\right)^2\right\}, \quad \text{(B3)}$$

where the three last terms are the pull terms (penalty terms) associated to the nuisance parameters and the σ_k are the prior uncertainties assumed for each systematic error ξ_k. Unless otherwise stated, for conventional neutrino beams we set the priors on the systematic uncertainties to the following values:

$$\sigma_\phi = 5\%; \qquad \sigma_{\bar{\nu}/\nu} = 10\%; \qquad \sigma_{\rm bg} = 10\%. \tag{B4}$$

In some cases we will show how the results change when σ_ϕ is increased to 15% (see Figs. 5 and 6). We have checked that this is the prior uncertainty which generally has the larger impact on the results of our analysis for the LBNE and T2HK setups.

The IDS-NF, on the other hand, is less affected by systematic errors: Any beam-related uncertainties will be small, since the flux can be computed analytically. Moreover, the availability of both electron and muon neutrino flavors at the near detector would allow one to determine their cross sections very precisely. We have chosen to use the same systematics implementation [Eqs. (B2) and (B3)] for this facility as for conventional beam experiments in order to ease the comparison between different facilities. However, in this case we assume that the near detector will generally do a better job canceling systematic uncertainties and therefore use the following priors:

$$\sigma_\phi = 3\%; \quad \sigma_{\bar{\nu}/\nu} = 5\%; \quad \sigma_{\rm bg} = 10\%; \quad \sigma_\tau = 30\%. \tag{B5}$$

Here, σ_τ refers in particular to the prior uncertainty associated to the ν_τ interaction cross section (which affects the backgrounds coming from τ contamination only [69,70]), while $\sigma_{\rm bg}$ is used for all the other background contributions. We have checked that the σ_τ prior uncertainty has the largest impact on the results for the IDS-NF setup used in this work. Its impact on the results for $\sin^2\theta_{23}$ is shown in Fig. 7.

Finally, marginalization is also performed over the oscillation parameters and the matter density. Unless otherwise stated, the following true values are assumed for the solar mixing parameters, θ_{13} and the atmospheric mass splitting:

$$\theta_{12} = 33.2°, \qquad \Delta m^2_{21} = 7.50 \times 10^{-5}\ \text{eV}^2,$$
$$\theta_{13} = 9.2°, \qquad \Delta m^2_{31} = 2.4 \times 10^{-3}\ \text{eV}^2 (\text{NH}),$$

while the assumed true values of θ_{23} and δ will be specified in each case. NH stands for normal hierarchy, i.e., $m_3 > m_1$. For each of the parameters which are marginalized over, a penalty term is added to the χ^2 in Eq. (B3) in the same way as it was done for the systematic uncertainties, and the global minimum is searched for.

Marginalization is always performed over the oscillation parameters not shown in each plot, by using Gaussian priors with the following 1σ errors: 3% for the solar oscillation parameters; 4% for the atmospheric mass splitting; 0.005 for $\sin^2 2\theta_{13}$, and 0.08 for $\sin^2 2\theta_{23}$. The values chosen for the solar and atmospheric mass splitting are in agreement with the current 1σ errors from global fits; see, for instance, Refs. [35–37]. For $\sin^2 2\theta_{13}$ we have used the precision expected at the end of the running of Daya Bay, assuming it is limited by their systematic error [73]. For $\sin^2 2\theta_{23}$, on the other hand, we use a value which lies roughly in between the current precision achieved at T2K and MINOS and the T2K systematic uncertainty for this parameter; see Refs. [32,74]. Unless otherwise stated, δ is left completely free during marginalization (i.e., no prior is assumed for this parameter). Finally, the value of the matter density is set according to the PREM profile [75,76], and a 2% prior uncertainty is assumed for this parameter.

[1] H. Nunokawa, S. J. Parke, and J. W. Valle, Prog. Part. Nucl. Phys. **60**, 338 (2008).
[2] M. Fukugita and T. Yanagida, Phys. Lett. B **174**, 45 (1986).
[3] F. An *et al.* (Daya Bay Collaboration), Phys. Rev. Lett. **112**, 061801 (2014).
[4] Y. Abe *et al.* (Double Chooz Collaboration), Phys. Rev. D **86**, 052008 (2012).
[5] S.-H. Seo (RENO Collaboration), arXiv:1312.4111.
[6] H. Minakata, H. Sugiyama, O. Yasuda, K. Inoue, and F. Suekane, Phys. Rev. D **68**, 033017 (2003).
[7] B. Aharmim *et al.* (SNO Collaboration), Phys. Rev. C **88**, 025501 (2013).
[8] R. Robertson, Prog. Part. Nucl. Phys. **57**, 90 (2006).
[9] A. Gando *et al.* (KamLAND Collaboration), Phys. Rev. D **88**, 033001 (2013).
[10] Y.-F. Li, J. Cao, Y. Wang, and L. Zhan, Phys. Rev. D **88**, 013008 (2013).
[11] C. D. Shin and K. K. Joo, Adv. High Energy Phys. **2014**, 320287 (2014).
[12] H. Minakata, M. Sonoyama, and H. Sugiyama, Phys. Rev. D **70**, 113012 (2004).
[13] H. Minakata and S. J. Parke, Phys. Rev. D **87**, 113005 (2013).
[14] K. Abe *et al.*, arXiv:1109.3262.
[15] C. Adams *et al.* (LBNE Collaboration), arXiv:1307.7335.
[16] S. K. Agarwalla, P. Huber, J. Tang, and W. Winter, J. High Energy Phys. 01 (2011) 120.
[17] IDS-NF Collaboration, International Design Study for a Neutrino Factory, https://www.ids-nf.org/wiki/FrontPage.
[18] E. Baussan *et al.*, arXiv:1212.5048.
[19] E. Baussan *et al.* (ESSnuSB Collaboration), Nucl. Phys. **B885**, 127 (2014).
[20] J. Burguet-Castell, M. Gavela, J. Gomez-Cadenas, P. Hernandez, and O. Mena, Nucl. Phys. **B608**, 301 (2001).

[21] G. L. Fogli and E. Lisi, Phys. Rev. D **54**, 3667 (1996).
[22] V. Barger, D. Marfatia, and K. Whisnant, Phys. Rev. D **65**, 073023 (2002).
[23] A. Donini, D. Meloni, and S. Rigolin, J. High Energy Phys. 06 (2004) 011.
[24] A. Chatterjee, P. Ghoshal, S. Goswami, and S. K. Raut, J. High Energy Phys. 06 (2013) 010.
[25] H. Minakata and H. Nunokawa, J. High Energy Phys. 10 (2001) 001.
[26] P. Huber, M. Lindner, and W. Winter, Nucl. Phys. **B645**, 3 (2002).
[27] K. Hiraide, H. Minakata, T. Nakaya, H. Nunokawa, H. Sugiyama, W. Teves, and R. Zukanovich Funchal, Phys. Rev. D **73**, 093008 (2006).
[28] S. K. Raut, Mod. Phys. Lett. A **28**, 1350093 (2013).
[29] H. Nunokawa, S. J. Parke, and R. Zukanovich Funchal, Phys. Rev. D **72**, 013009 (2005).
[30] R. Wendell *et al.* (Super-Kamiokande Collaboration), Phys. Rev. D **81**, 092004 (2010).
[31] M. Ahn *et al.* (K2K Collaboration), Phys. Rev. D **74**, 072003 (2006).
[32] P. Adamson *et al.* (MINOS Collaboration), Phys. Rev. Lett. **106**, 181801 (2011).
[33] K. Abe *et al.* (T2K Collaboration), Phys. Rev. Lett. **112**, 181801 (2014).
[34] D. Ayres *et al.* (NOvA Collaboration), arXiv:hep-ex/0503053.
[35] M. Gonzalez-Garcia, M. Maltoni, J. Salvado, and T. Schwetz, J. High Energy Phys. 12 (2012) 123; http://www.nu-fit.org/.
[36] F. Capozzi, G. L. Fogli, E. Lisi, A. Marrone, D. Montanino, and A. Palazzo, Phys. Rev. D **89**, 093018 (2014).
[37] D. Forero, M. Tortola, and J. Valle, arXiv:1405.7540 [Phys. Rev. D (to be published)].
[38] A. Minamino, in Proceedings of the KEK Seminar, 2014 (unpublished), http://www.t2k.org/docs/talk/144/new-results-from-t2k-pdf.
[39] K. Abe *et al.* (T2K Collaboration), Nucl. Instrum. Methods Phys. Res., Sect. A **659**, 106 (2011).
[40] T. Akiri *et al.* (LBNE Collaboration), arXiv:1110.6249.
[41] LBNE Conceptual Design Report, Vol. 1, https://sharepoint.fnal.gov/project/lbne/LBNE%20at%20Work/SitePages/Reports%20and%20Documents.aspx.
[42] A. Stahl *et al.*, Report Nos. CERN-SPSC-2012-021, SPSC-EOI-007, 2012.
[43] S. Choubey *et al.* (IDS-NF Collaboration), arXiv:1112.2853.
[44] E. Fernandez Martinez, T. Li, S. Pascoli, and O. Mena, Phys. Rev. D **81**, 073010 (2010).
[45] E. Christensen, P. Coloma, and P. Huber, Phys. Rev. Lett. **111**, 061803 (2013).
[46] W. J. Marciano, arXiv:hep-ph/0108181.
[47] M. Diwan *et al.*, arXiv:hep-ex/0211001.
[48] M. Ishitsuka, T. Kajita, H. Minakata, and H. Nunokawa, Phys. Rev. D **72**, 033003 (2005).
[49] P. Coloma and E. Fernandez-Martinez, J. High Energy Phys. 04 (2012) 089.
[50] A. Donini, E. Fernandez-Martinez, and S. Rigolin, Phys. Lett. B **621**, 276 (2005).
[51] A. Donini, D. Meloni, and S. Rigolin, Eur. Phys. J. C **45**, 73 (2006).
[52] A. Donini, E. Fernandez-Martinez, D. Meloni, and S. Rigolin, Nucl. Phys. **B743**, 41 (2006).
[53] M. Gonzalez-Garcia, M. Maltoni, and A. Y. Smirnov, Phys. Rev. D **70**, 093005 (2004).
[54] K. B. M. Mahn and M. H. Shaevitz, Int. J. Mod. Phys. A **21**, 3825 (2006).
[55] P. Huber, M. Lindner, M. Rolinec, T. Schwetz, and W. Winter, Phys. Rev. D **70**, 073014 (2004).
[56] S. Choubey and P. Roy, Phys. Rev. D **73**, 013006 (2006).
[57] S. K. Agarwalla, S. Prakash, and S. U. Sankar, J. High Energy Phys. 07 (2013) 131.
[58] P. Machado, H. Minakata, H. Nunokawa, and R. Zukanovich Funchal, J. High Energy Phys. 05 (2014) 109.
[59] S. Choubey and A. Ghosh, J. High Energy Phys. 11 (2013) 166.
[60] M. Ghosh, P. Ghoshal, S. Goswami, and S. K. Raut, Nucl. Phys. **B884**, 274 (2014).
[61] C. Bronner and L. Cremonesi, in Proceedings of the Fourth Open Meeting for the Hyper-Kamiokande Project (unpublished), http://indico.ipmu.jp/indico/conferenceDisplay.py?confId=29.
[62] P. Coloma, P. Huber, J. Kopp, and W. Winter, Phys. Rev. D **87**, 033004 (2013).
[63] P. Coloma, A. Donini, E. Fernandez-Martinez, and P. Hernandez, J. High Energy Phys. 06 (2012) 073.
[64] P. Huber, M. Mezzetto, and T. Schwetz, J. High Energy Phys. 03 (2008) 021.
[65] L. Agostino, M. Buizza-Avanzini, M. Dracos, D. Duchesneau, M. Marafini, M. Mezzetto, L. Mosca, T. Patzak, A. Tonazzo, and N. Vassilopoulos (MEMPHYS Collaboration), J. Cosmol. Astropart. Phys. 01 (2013) 024.
[66] A. de Bellefon *et al.*, arXiv:hep-ex/0607026.
[67] R. Bayes, A. Laing, F. J. P. Soler, A. Cervera Villanueva, J. J. Gómez Cadenas, P. Hernández, J. Martín-Albo, and J. Burguet-Castell, Phys. Rev. D **86**, 093015 (2012).
[68] Neutrino Factory Reference Design report (IDS-NF Collaboration) (to be published).
[69] D. Indumathi and N. Sinha, Phys. Rev. D **80**, 113012 (2009).
[70] A. Donini, J. Gomez Cadenas, and D. Meloni, J. High Energy Phys. 02 (2011) 095.
[71] P. Huber, M. Lindner, and W. Winter, Comput. Phys. Commun. **167**, 195 (2005).
[72] P. Huber, J. Kopp, M. Lindner, M. Rolinec, and W. Winter, Comput. Phys. Commun. **177**, 432 (2007).
[73] D. A. Dwyer (Daya Bay Collaboration), Nucl. Phys. B, Proc. Suppl. **235–236**, 30 (2013).
[74] K. Abe *et al.* (T2K Collaboration), Phys. Rev. D **85**, 031103 (2012).
[75] F. Stacey, *Physics of the Earth*, 2nd ed. (Wiley, New York, 1977).
[76] A. Dziewonski and D. Anderson, Phys. Earth Planet. Inter. **25**, 297 (1981).